

Pore Size and Porosity Dependent Zeta Potentials of Mesoporous Silica Nanoparticles

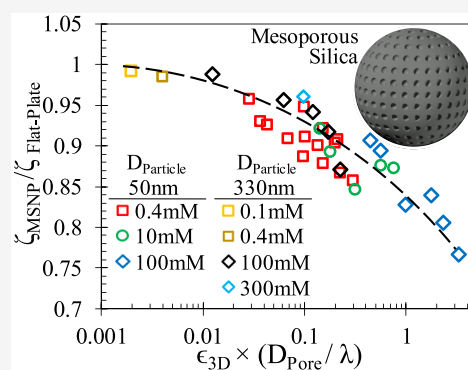
Fetiye Esin Yakin, Murat Barisik,* and Tumcan Sen

 Cite This: *J. Phys. Chem. C* 2020, 124, 19579–19587 Read Online

ACCESS |

 Metrics & More Article Recommendations

ABSTRACT: Mesoporous silica nanoparticles (MSNPs) are synthesized in the various forms of porous structures according to an application's needs, while their zeta potentials play a major role in their function. We show that variation in pore size and/or porosity yields a substantial decrease in MSNP zeta potential up to 25% lower than the theoretical zeta potential predictions for a flat surface at the corresponding ionic conditions in moderate pH range. By considering surface chemistry as a function of local ionic conditions (charge regulation), we calculated local zeta potentials around the MSNP which showed variation between pore openings and solid surfaces. Through a systematic study, we evaluated an average three-dimensional zeta potential for MSNPs with various conditions, based on the ratio of the area covered by pore openings to the rest of the MSNP surface area as a function of three-dimensional porosity and pore size. Results show that the high overlap of ionic layers inside the pores creates electric potentials close to zeta potential of the remaining surface, but large pore size and/or high ionic salt concentration yields divergence. We characterized the variation of MSNP zeta potential in terms of porosity (ϵ_{3D}), pore size (D_{pore}), and ionic condition quantified by Debye length (λ) and obtained unified behavior as a function of the nondimensional group of $\epsilon_{3D}(D_{\text{pore}}/\lambda)$. For $\epsilon_{3D}(D_{\text{pore}}/\lambda) < 0.01$, MSNP zeta potential remains similar to flat plate predictions, but it decreases by increasing $\epsilon_{3D}(D_{\text{pore}}/\lambda)$ value. The influence of pore entrances on surface zeta potential increases nonlinearly by the increase of porosity and/or decrease of EDL overlap, similar to a change of area to volume ratio. The current findings are important for the understanding and further control of mesoporous particle transport in various promising and groundbreaking applications such as targeted drug delivery.



1. INTRODUCTION

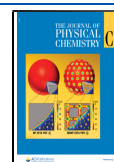
Mesoporous silica nanoparticles (MSNPs) are a key material for biosensing,^{1,2} cell tracing,^{3,4} bioimaging,^{5,6} biodiagnosing,^{7,8} biocatalysis,^{9,10} and targeted anticancer agent^{11,12} or drug^{13,14} delivery in biotechnological applications. Highly ordered MSNPs in various sizes have been synthesized with uniform and tunable pore sizes.^{15,16} The structural parameters as well as the electric charge properties of both internal/external surfaces are the main determining factors in an MSNP's function. However, characterization of the zeta potential of an MSNP as a function of its structural porous parameters such as pore size and porosity is absent in the literature.

MSNPs with diameters less than 500 nm with pore sizes ranging from 2 to 50 nm are great candidates for drug delivery applications^{17–19} as they can transport a large amount of drugs into selective organs and tissues. Such targeted drug delivery systems are very promising and groundbreaking for cancer treatment therapies.^{20–22} With the advanced synthesis techniques, MSNPs can be designed to load/carry the required amount of drug, enter only the targeted type of cell, and remain inside the cell long enough to release the required drug without being destroyed. Such a specific nanocarrier can be

obtained by adjusting the size,²³ morphology,²⁴ and pore structure,²⁵ and more importantly, by calibrating the electrokinetic properties.²⁶ For example, drug loading-releasing mechanisms depend on porosity and pore sizes and also on surface charge.²⁷ Surface charge is found to be important in the nanofluidic transport of nanoparticles.^{28,29} Cellular uptake, endosomal escape, and undesired protein corona formation were all found to be strongly dependent on mesoporous parameters as well as surface charge properties.¹¹ However, for a mesoporous system, the internal porous parameters determine the zeta potential around the particle, which has been overlooked in the current literature.

A solid surface in an electrolyte develops a surface charge due to the association/disassociation reactions on the surface

Received: May 21, 2020
Revised: August 7, 2020
Published: August 10, 2020



and the adsorption of ions. This surface charge can be analytically calculated as a function of ionic concentration and pH by describing the resulting electric double layer (EDL) with Boltzmann Distribution (BD).³⁰ Most researchers use the classical Poisson–Boltzmann (PB) solutions to calculate a surface zeta potential for a nanoparticle as a constant property of the corresponding material.^{31–33} However, this description is not valid for MSNPs because a particle's surface is curved and uneven due to pore openings. First, a decrease in overall particle size develops curvature effects that cause the ionic condition around the particle to diverge from a flat surface.^{34–36} Curvature effects are due to the decreased surface to volume ratio by the decrease in particle diameter as observed through several studies.^{37,38} Second, the electric potential at the pore openings around the particle's surface will be different than the condition of the surface itself so that the average zeta potential around the particle differs from a smooth nonporous surface.^{39–41} This variation is basically determined by the ionic conditions inside the mesoporous system as a function of pore size and porosity. As a result, the ionic conditions and the resulting zeta potential around the MSNP form as a function of particle size, pore size, and porosity different than the existing flat and smooth surface theory.

The above-described surface charging mechanisms can only be calculated by considering the natural surface physicochemistry through surface charge regulation (CR) models incorporated with Poisson–Nernst–Planck (PNP) equations.^{42,43} CR was first identified by Ninham and Parsegian⁴⁴ and later observed by multiple experiments in surface force measurements by colloids^{45,46} and AFM.^{47,48} Since then, researchers have attempted to apply CR in calculations using active charge models as boundary conditions to resolve surface charging of silica nanochannels,^{49–51} nanopores,^{52–57} mesoporous systems,^{58,59} and nanoparticles.^{34,43,60} Using this systematic approach, we characterized surface charging of SNPs and presented that the SNP surface charge depends on the size of the nanoparticle.³⁴ Just recently, we also described the effect of surface roughness/patterning on the surface charge of SNPs³⁵ and planar surfaces⁶¹ where surface charge shows local variation and the average of it becomes different than predictions for a flat surface condition.

The aim of this work is to extend our earlier experience toward investigation of the effects of the internal mesoporous system on MSNP surface charging. We study different size MSNPs at various porous parameters and ionic conditions. A multi-ion charge regulation model is used with PNP. We systematically vary the particle size, pore size, porosity, and ionic concentration to study local electric potential around an MSNP.

2. THEORETICAL BACKGROUND AND NUMERICAL MODEL

Highly ordered MSNPs with a rich variety and precise control over shape and size of mesoporous systems have been synthesized by multiple research groups, such as MCM (Mobil Composition of Matter),^{62,63} KIT (Korea Institute of Technology),⁶⁴ SBA (Santa Barbara Amorphous),^{65,66} and FDU (Fudan University in Shanghai).⁶⁷ Varying synthesis conditions yield various forms of mesoporous silica with very well-ordered arrangements in porous geometries. Recently, cubic silicates with highly ordered periodic structures repeating in either two- or three-dimensions received the most attention that multiple studies synthesized high-quality cubic meso-

porous materials with a desired structure. For instance, ordered periodic pore arrays of SBA-16 can easily be controlled such that desired pore diameter and pore throat size can be obtained by the synthesis temperature and time.⁶⁸ Figure 1a

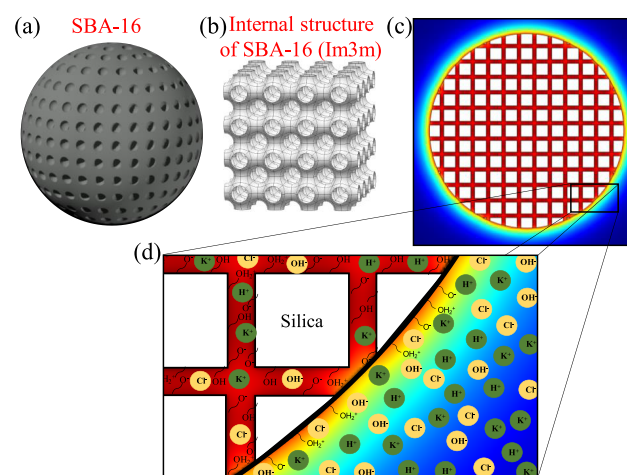


Figure 1. Schematic illustration of (a) SBA-16, (b) internal structure of SBA-16 in the form of cubic Im3m, (c) representative two-dimensional cross-section through the center line of SBA-16, and (d) close-up view of the solution domain consisting of silica surfaces and four different ionic species.

and b provides simple representations of the SBA-16 (Im3m) and its internal structure which is similar to the experimentally determined structure by electron crystallography⁶⁹ as well as earlier studies^{16,70–72} which obtained structures at different porosities. We simplified such a three-dimensional structure into a two-dimensional representation as described in Figure 1c.

We used KCl solution as our electrolyte which contains H^+ , K^+ , Cl^- , and OH^- ions with the i th species' bulk concentration and valence being c_{i0} and z_i ($i = 1$ for H^+ ; $i = 2$ for K^+ ; $i = 3$ for Cl^- ; $i = 4$ for OH^-). Bulk concentrations of these species are chosen so that the electroneutrality condition is satisfied. Hence, $c_{10} = 10^{-pH+3}$, $c_{40} = -(14-pH)+3$, $c_{20} = c_{KCL}$, and $c_{30} = C_{KCL} + c_{10} - c_{40}$ for $pH \leq 7$; $c_{20} = C_{KCL} - c_{10} + c_{40}$, and $c_{30} = c_{KCL}$ for $pH > 7$.^{73,74} The Debye length that characterizes the electric double layer can be calculated as $\lambda = 1/k = \sqrt{\epsilon_0 \epsilon_r k_B T / N_A e^2 \sum c_{i0} z_i^2}$ where ϵ_0 and ϵ_r are the permittivity of vacuum and dielectric constant of the electrolyte, respectively. Boltzmann and Avogadro constants are denoted by k_B and N_A , respectively, while T is the temperature and e is the elementary charge.

We used Poisson–Nernst–Planck (PNP) equations to calculate electrostatic potential and the ion flux as given in eqs 1 and 2. In eqs 1 and 2, ψ is the electric potential, N_i is the flux density, D_i is the diffusivity; F and R are the Faraday and the universal gas constants, respectively.

$$-\epsilon_0 \epsilon_r \nabla^2 \psi = F \sum z_i c_i \quad (1)$$

$$\nabla \cdot \left(-D_i \nabla c_i - z_i \frac{D_i}{RT} F c_i \nabla \psi \right) = 0 \quad (2)$$

The electric potential and ionic concentrations described by PNP equations are numerically calculated in 2D Cartesian coordinates based on finite element method with COMSOL

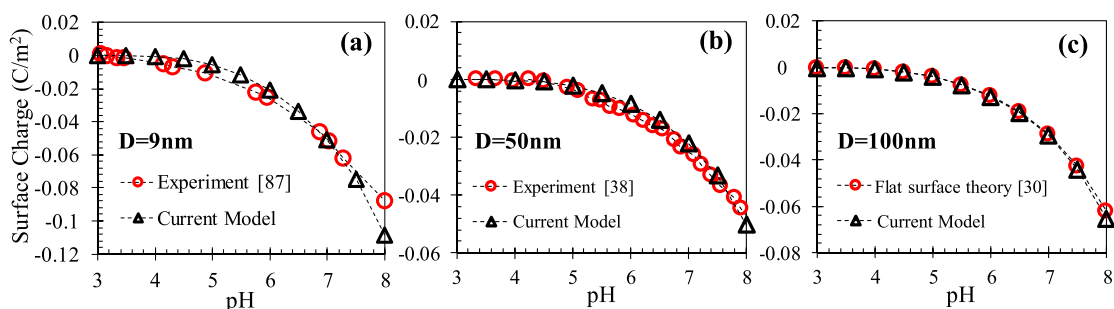
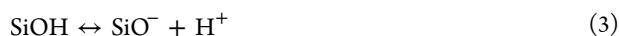


Figure 2. Comparison between numerical results and experimental/theoretical data of (a) Brown et al.⁸⁷ for a 9 nm flat silica nanoparticle in 50 mM KCl (corresponding simulations were performed using $D_p = 9$ nm, $C_{KCl} = 50$ mM, $\Gamma_{total} = 4.75$ sites/nm², $pK_A = -\log K_A = 7$, and $pK_B = -\log K_B = 1.9$); (b) Kobayashi et al.³⁸ for a 50 nm flat silica nanoparticle in 10 mM KCl, respectively (corresponding simulations were performed using $D_p = 50$ nm, $C_{KCl} = 10$ mM, $\Gamma_{total} = 8$ sites/nm², $pK_A = -\log K_A = 7.6$, and $pK_B = -\log K_B = 1.9$); (c) flat surface theory³⁰ for a silica surface in 10 mM KCl (corresponding simulations were performed using $D_p = 100$ nm, $C_{KCl} = 10$ mM, $\Gamma_{total} = 4.816$ sites/nm², $pK_A = -\log K_A = 7$, and $pK_B = -\log K_B = 1.9$). Parameters are adopted from corresponding studies.

Multiphysics (www.comsol.com). The solution is coupled with the charge regulation model to calculate the interaction of ions and silanol groups on the surface as



The equilibrium constants of these reactions are calculated by using the site density of the silanol groups (Γ_{SiO^-} , Γ_{SiOH} , and $\Gamma_{\text{SiOH}_2^+}$) and the hydrogen concentration at the interface $[\text{H}^+]_w$:

$$K_A = \frac{\Gamma_{\text{SiO}^-}[\text{H}^+]_w}{\Gamma_{\text{SiOH}}}, \quad K_B = \frac{\Gamma_{\text{SiOH}_2^+}}{\Gamma_{\text{SiOH}}[\text{H}^+]_w} \quad (5)$$

Using these parameters, the surface charge density, used as a boundary condition on the solid surfaces to model charge regulation nature of silica surfaces, is calculated as

$$\sigma_w = -\frac{F\Gamma_{total}}{N_A} \frac{K_A - K_B[\text{H}^+]_w^2}{K_A + [\text{H}^+]_w + K_B[\text{H}^+]_w^2} \quad (6)$$

For most of the cases, we simulated a moderate pH level of 6 at the room temperature of 300 K. The literature showed us that MSNP applications mostly take place at an average pH value of 6. We also studied different pH conditions between 6 and 8 as the pH levels of human blood, most human organs, and most tumor cells vary between pH 6 and 8.^{75–79} Total site density (Γ_{total}) is selected as 4.816 sites/nm² while the equilibrium constants pK_A and pK_B are taken as 7 and 1.9 which are validated by experiments in our earlier study.³⁵ These charge regulation model parameters also very similar to those reported in the literature in a range of $\Gamma_{total} = 4.6–4.9$ sites/nm², $pK_A = 6.3–7.4$ and $pK_B = 0–3$ by many studies.^{80–86} The diffusivities of H^+ , K^+ , Cl^- , and OH^- ions are 9.31×10^{-9} , 1.957×10^{-9} , 2.032×10^{-9} , and 5.3×10^{-9} m²/s, respectively. The following values are used for the constants: $\epsilon_0\epsilon_r = 7.08 \times 10^{-10}$ F/m, $R = 8.31$ J/(mol·K), $F = 96485$ C/mol. We tested the numerical procedure by comparing its results with the available experimental measurements of Brown et al.⁸⁷ for a 9 nm flat silica nanoparticle in 50 mM KCl solution and Kobayashi et al.³⁸ for a 50 nm flat silica nanoparticle in 10 mM KCl solution. We further compared our model with the theoretical calculations for a 100 nm nanoparticle at which surface charging is expected to develop similar to a flat surface theory.³⁰ Figure 2 presents the surface charge density values for pH range from 3 to 8. Numerical

results show good agreement with the experimental/theoretical values.

3. RESULTS AND DISCUSSION

We started our investigations with a large particle of 330 nm in diameter. We simulated the high ionic concentration of 100 mM to obtain a low EDL thickness of $\lambda = 0.97$ nm. In this case, we simply varied the pore size while keeping the porosity of the two-dimensional cross-section at a constant value of $\epsilon_{2D} = 0.166$. In addition, we also maintained the perimeter occupied by the pore entrances constant between these systems of different pore sizes. The electric potential contours and local potential values measured around the particle surface are given in Figure 3. We only presented electric potential through a 45° arc-length since the rest of surface is either identical or

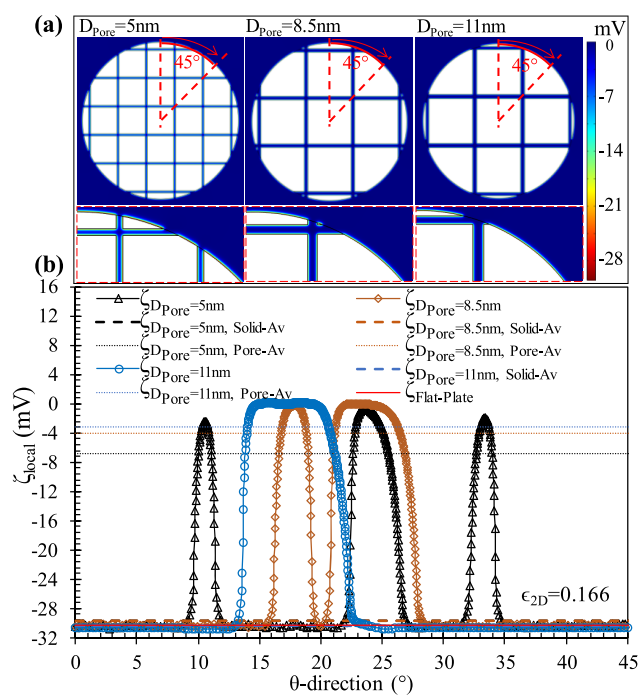


Figure 3. (a) Electric potential contours presenting the cross-section of each case. (b) Local potential distribution around the $D_{particle} = 330$ nm MSNPs having different pore sizes of $D_{pore} = 5, 8.5,$ and 11 nm while the porosity in the two-dimensional cross-section was kept constant at $\epsilon_{2D} = 0.166$.

symmetric to this region. Electric potential contours for this very low EDL thickness do not show much, but this reveals the variation of the mesoporous structure. We observed important physics from the potentials measured around the particle surface. The surface zeta potential measured on solid parts are identical to analytical PB calculations of a flat smooth surface. This result is expected since the curvature effects do not develop for particle diameters higher than ~ 50 nm.³⁴ On the other hand, sudden jumps are observed at the pore openings where the absolute value of electric potential undergoes rapid decreases. For the case of pore size equal to 11 nm, electric potential inside the pores is equal to a reservoir value of 0 mV. However, with the decrease in pore size to $D_{\text{pore}} = 5$ nm, EDLs from opposite pore surfaces start to overlap creating electric potentials different than zero inside the pores.

In Figure 3, we also calculated the average of the electric potentials developing through every pore opening as well as through the remaining solid surfaces around the MSNPs. For the $D_{\text{pore}} = 11$ nm case, the average potential of pores and solids are equal to reservoir value of 0 mV and theoretical flat surface value, respectively. Eventually, this specific case provides us the ground at which the electric potentials are equal to the values of known simple situations without curvature and EDL overlap effects. However, with the decrease in pore size, absolute value of the average potential of pores increases when the EDL overlap starts. The average potential through the solid parts also starts to deviate from the theory with decreasing pore size due to increased number of surface pores bringing pore corner effects, even though the curvature effects are negligible at this particle diameter of 330 nm. In order to develop these discussions specific to pore size effects, we should underline again that we kept the ϵ_{2D} and the perimeter occupied by the pore entrances constant for these different pore size cases during their design.

Next, in Figure 4, we studied the increase of porosity. For the case of $D_{\text{particle}} = 330$ nm with $D_{\text{pore}} = 5$ nm at $C_{\text{KCl}} = 100$ mM, we varied the two-dimensional porosity as $\epsilon_{2D} = 0.166$, 0.345, and 0.47. The number of surface pores increases with the increase of porosity. The electric potential at the pore mouths remained similar at negligible potential values close to 0 mV that the average pore potential is mostly unaffected by porosity change. This is expected since the condition of EDL overlap remained same for these cases at constant pore size and salt concentration. The major effect of porosity increase is onto average potential of solid sections; the increase of pores creates higher corner effects by the increase of porosity and the absolute value of average surface potential decreases. Detailed discussion about the “corner effects” onto surface charge equilibrium of nanosystems can be found in our earlier study describing surface charging of a single pore with various pore lengths.⁸⁸

The influence of salt concentration is studied in Figure 5. Four different salt concentrations of $C_{\text{KCl}} = 0.1$, 0.4, 100, and 300 mM were created as the electrolyte for the case of $D_{\text{particle}} = 330$ nm with $D_{\text{pore}} = 5$ nm and $\epsilon_{2D} = 0.166$. With the decrease of salt concentration, EDL thickness increases creating strong EDL overlap. Increasing overlap yields electric potential inside the pores which becomes very different than the reservoir condition, and actually, potential at the pores approaches the potential value of the solid surfaces. At the same time, decreasing the salt concentration increases the absolute value of electric potential on solid surfaces similar to theoretical predictions. Potential on solid surfaces still remains

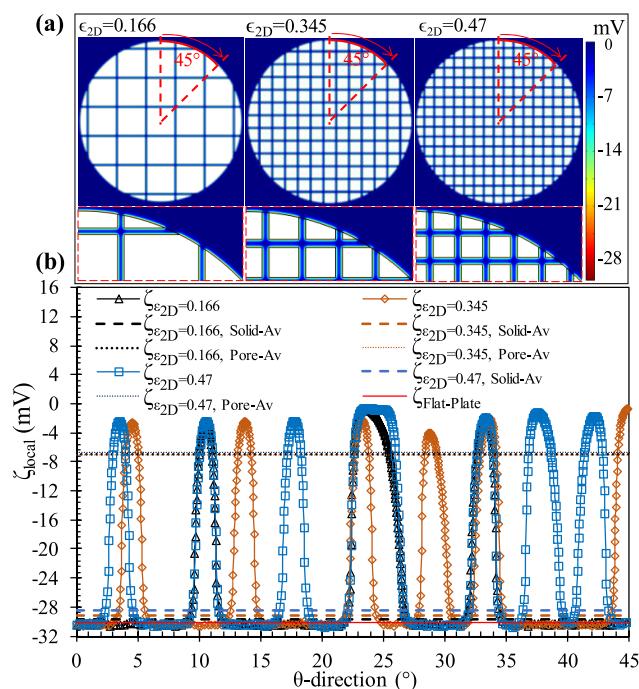


Figure 4. (a) Electric potential contours presenting the cross-section of each case. (b) Local potential distribution around the $D_{\text{particle}} = 330$ nm MSNPs of $D_{\text{pore}} = 5$ nm with different $\epsilon_{2D} = 0.166$, 0.345, and 0.47.

very close to calculations of the flat surface theory. Electric potential distributions normalized by the corresponding theory given in Figure 5c. For the lowest ionic concentration of 0.1 mM, local variation of electric potential through solid surface, pore corners, and pore bulk almost disappears. Hence, zeta potential of this 330 nm diameter MSNP (no curvature effects) at high EDL overlap (low salt concentration and/or small pore size) develops no mesoporous related effects and approaches flat surface theory.

We studied variations in pH in Figure 6. For the case of $D_{\text{particle}} = 330$ nm with $D_{\text{pore}} = 5$ nm and $\epsilon_{2D} = 0.166$ at $C_{\text{KCl}} = 0.1$ we simulated different pH conditions of 6, 7, and 8. Increasing pH increases the absolute value of electric potential on solid surfaces similar to theoretical predictions. At the same time, EDL overlap decreases by the increase of pH yielding pore electric potential approach back to reservoir conditions. Electric potential distributions normalized by the corresponding theory are given in Figure 6c. The local variation of electric potential increases by increasing pH which creates slightly higher difference between solid parts and pore entrances.

Next, we studied the decrease of particle size in Figure 7. We chose the $D_{\text{pore}} = 5$ nm with $C_{\text{KCl}} = 0.1$ mM which develops high EDL overlap and pore potentials approach the potential value of solid parts. MSNPs with diameters $D_{\text{particle}} = 40$, 128, 166.5, 201.5, and 252 nm at $\epsilon_{2D} = 0.42$ were designed as illustrated in Figure 7a. Local electric potential distributions are given in Figure 7b. High absolute potential values are observed on solid parts while low values are at the pore mouths. The average potentials measured at the pores and solid regions normalized with the prediction of flat surface theory for $C_{\text{KCl}} = 0.1$ mM are given in Figure 7c for these different size MSNPs. With the decrease in particle diameter, the average pore potential mostly remains constant at 95% of the theoretical value; at this concentration, high EDL overlap

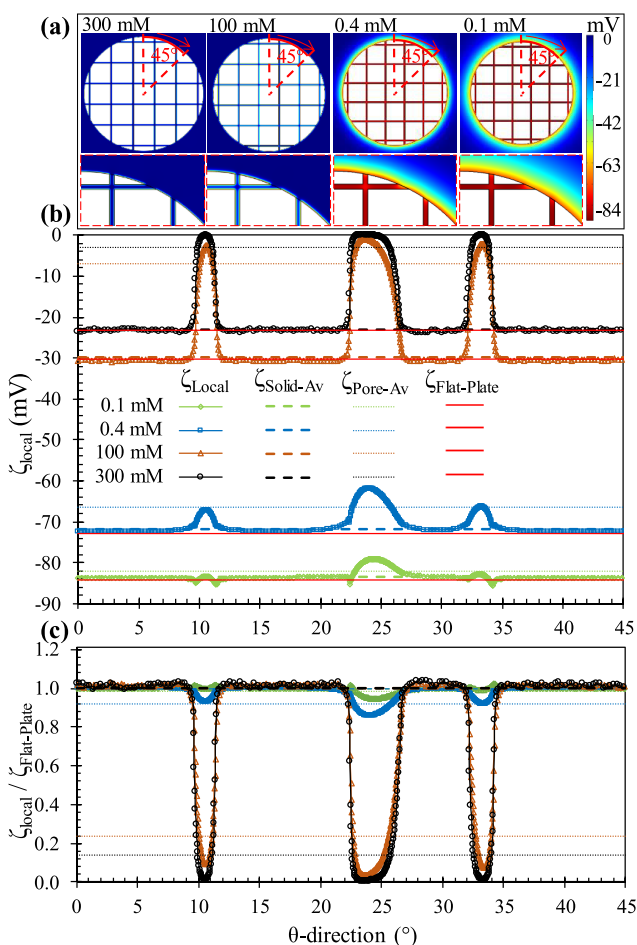


Figure 5. (a) Electric potential contours presenting the cross-section of each case. (b) Local potential distribution around the $D_{\text{particle}} = 330$ nm MSNPs of $D_{\text{pore}} = 5$ nm and $\epsilon_{2D} = 0.166$ at different $C_{\text{KCl}} = 0.1, 0.4, 100,$ and 300 mM. (c) Local variation of electric potentials normalized by corresponding flat plate theory values.

creates pore potential values close to surface value as we discussed earlier. On the other hand, a decrease in particle diameter has a strong influence on the average solid potential due to curvature effects; by decreasing the particle diameter below 150 nm, solid potential develops a 10% decrease at $D_{\text{particle}} = 40$ nm. Further decrease in particle diameter creates lower potentials.

We further investigated influence of pores size, porosity, and salt concentration for the case of a low particle diameter of with $D_{\text{pore}} = 50$ nm. In Figure 8a, b, and c, pore size varied as $D_{\text{pore}} = 3, 5, 8,$ and 10 nm for the case of $\epsilon_{2D} = 0.47$ at $C_{\text{KCl}} = 0.1$ mM. Similar to the influence of salt concentration, decrease in pore size increases the EDL overlap and yields an absolute value of pore potential increase, getting close to the solid values. The average values of the pore potentials and solid potentials are given in Figure 8c as a function of pore size. The normalized average pore potential decreases while the solid potential remains mostly constant for increasing pore size. We should underline once more that in order to understand the effect of pore size only, independent from other possible effects, we kept the perimeter covered by solid or pore regions constant between these cases. Figure 8d–f presents the influence of the porosity of the two-dimensional cross-section of the $D_{\text{pore}} = 5$ nm case at $C_{\text{KCl}} = 0.1$ mM. Similar to the earlier conclusion, a change in porosity increases the number

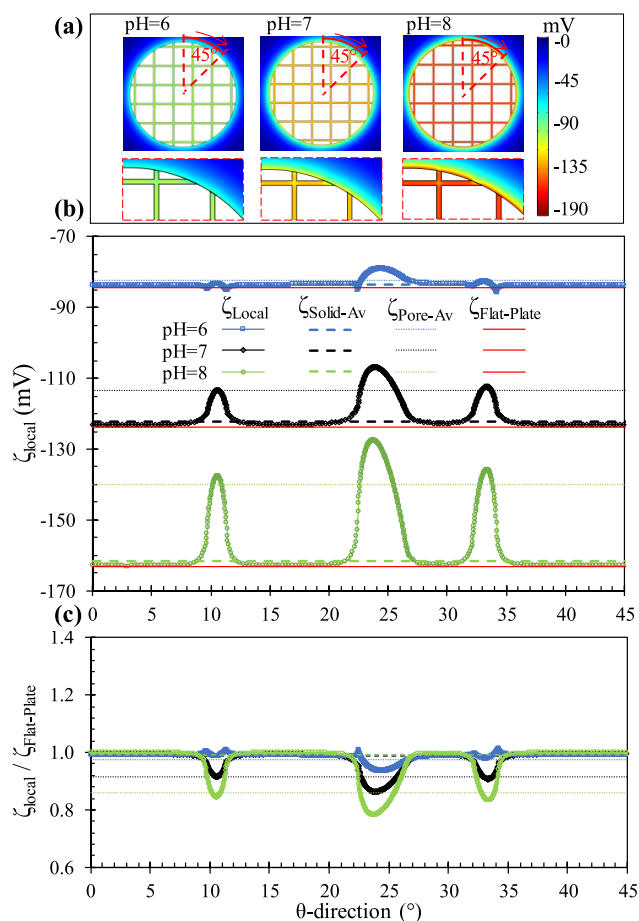


Figure 6. (a) Electric potential contours presenting the cross-section of each case. (b) Local potential distribution around the $D_{\text{particle}} = 330$ nm MSNPs of $D_{\text{pore}} = 5$ nm and $\epsilon_{2D} = 0.166$ at different pH values = 6, 7, and 8. (c) Local variation of electric potentials normalized by corresponding flat plate theory values.

of surface pores which creates strong pore corner effects decreasing pore and solid surface charging. The normalized average values in Figure 8f shows a decrease in both solid and pore potential.

Figure 8g–i shows the surface charging for different ionic conditions for the $D_{\text{pore}} = 5$ nm case at $\epsilon_{2D} = 0.67$. The increase of salt concentration decreases the EDL thickness that the average electric potential in pores decreases due to the decreasing EDL overlap. For the 100 mM case, the overlap in pores almost disappears so that potential reaches equilibrium with the reservoir at zero potential value. On the other hand, the potential on solid parts remains mostly constant, close to theoretical estimations.

Next, we defined and calculated an average zeta potential for three-dimensional MSNP surface using the electric potential calculations of two-dimensional cross-section of centerline. Figure 9 gives the representation of this system with an example of a 50 nm diameter MSNP with 5 nm pore size. Basically, the number of surface pore openings and the corresponding area covered by pores can be easily estimated from the two-dimensional cross-section of this spherical system. Using the average electric potentials calculated at the pores and on the remaining surfaces, an average potential can be calculated as

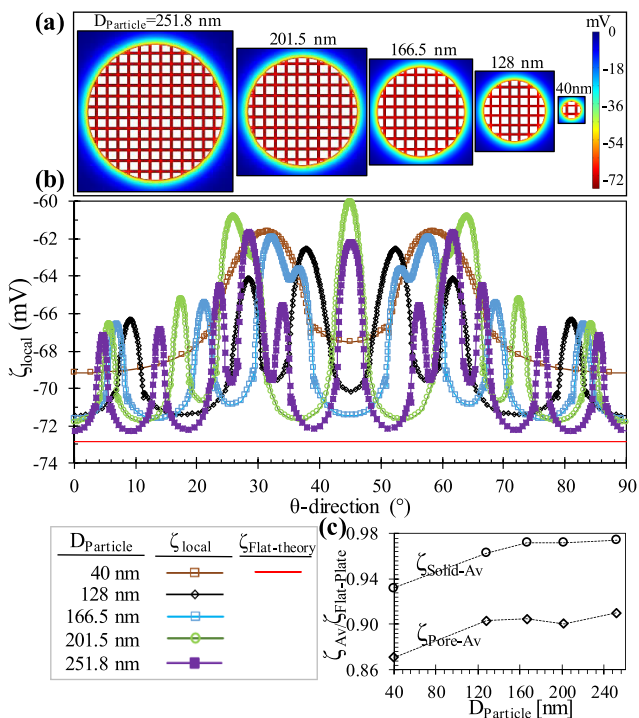


Figure 7. (a) Electric potential contours presenting the cross-section of each case. (b) Local potential distribution around the different size MSNPs of $D_{\text{particle}} = 40, 128, 166.5, 201.5,$ and 251.8 nm with $D_{\text{pore}} = 5$ nm and $\epsilon_{2D} = 0.42$. (c) Variation of the normalized average potential of pore mouths and solid parts as a function of particle diameter.

$$\zeta_{\text{MSNP}} = \zeta_{\text{solid,av}} \left(1 - N_{\text{pore}} \frac{D_{\text{pore}}^2}{4D_{\text{particle}}^2} \right) + \zeta_{\text{pore,av}} N_{\text{pore}} \frac{D_{\text{pore}}^2}{4D_{\text{particle}}^2} \quad (7)$$

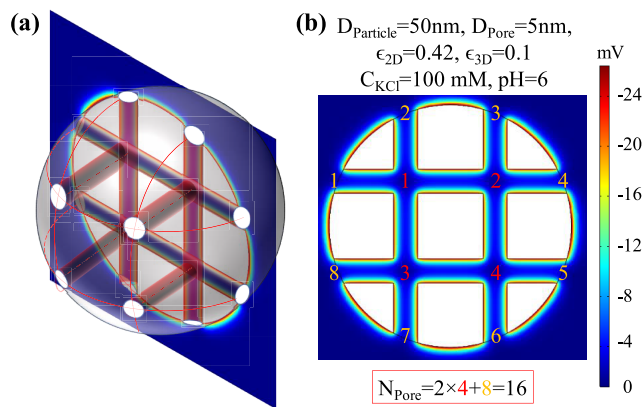


Figure 9. (a) Description of the two-dimensional representative cross-section from the spherical porous particle in three-dimensional extent. (b) Example calculation for number of pores of 50 nm diameter MSNP with 5 nm pore size.

where ζ_{MSNP} is the average zeta potential around three-dimensional mesoporous silica nanoparticle surface as a function of the average zeta potential on solid parts ($\zeta_{\text{solid,av}}$) and pores ($\zeta_{\text{pore,av}}$), number of pores on the surface (N_{pore}), and diameter of pores (D_{pore}) and particle itself (D_{particle}).

Additionally, a three-dimensional MSNP porosity is defined and calculated from the total volume of the porous system estimated by measuring the pore lengths from the two-dimensional cross section.

$$\epsilon_{3D} = \frac{N_{\text{pore}} L_{\text{pore,av}}}{2} \frac{3}{2} \frac{D_{\text{pore}}^2}{D_{\text{particle}}^3} \quad (8)$$

where ϵ_{3D} is the three-dimensional porosity of MSNP, and $L_{\text{pore,av}}$ is the average of lengths of the internal pores. Using eqs 7 and 8, we calculated the three-dimensional average zeta

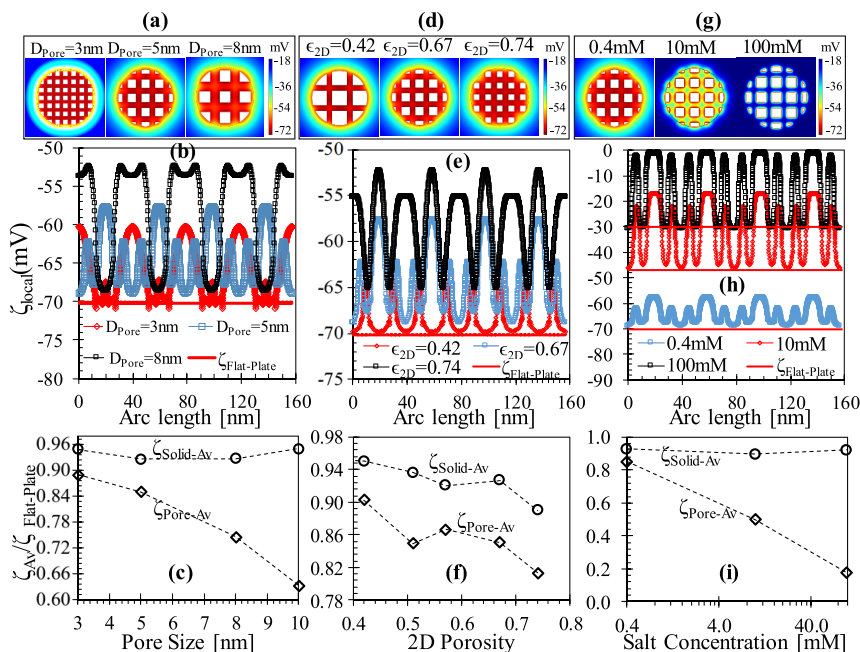


Figure 8. (a, d, g) Electric potential contours presenting the cross section of each case. (b, e, h) Local electric potential distribution around $D_{\text{particle}} = 50$ nm for various pore sizes, porosities, and salt concentrations. (c, f, i) Variation of the average potential of pore mouths and solid parts normalized by flat plate theory as a function of pore size, porosity, and salt concentration.

potential and porosity of all of the cases we studied above. Figure 10 presents variation of MSNP average zeta potential as

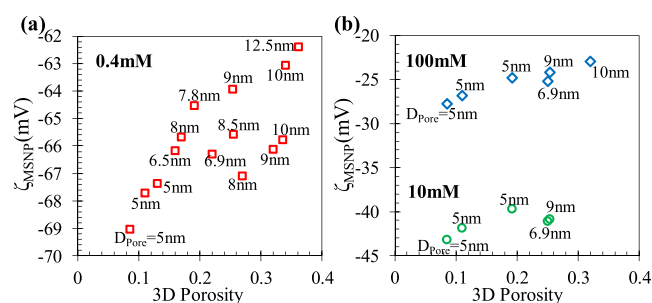


Figure 10. Average zeta potentials of 50 nm diameter MSNPs with various pore diameters and 3D porosities at different salt concentrations.

a function of porosity for particle diameter of 50 nm at various pore diameters and salt concentration. First, through 0.4 mM cases, an increase in pore size and/or 3D porosity yields a decrease of absolute MSNP surface zeta potential in Figure 10a. A similar behavior is observed for higher salt concentration cases of 10 and 100 mM in Figure 10b. However, a clear relationship between zeta potential and all these porous parameters appears hard to obtain. This shows that characterization based on 3D porosity only is not adequate.

Results show that a thorough understanding of MSNP zeta potential requires characterization of each charging mechanism in terms of porous parameters. First, in the current study set of $D_{\text{pores}} > 3$ nm, particle diameters are higher than 50 nm to attain systems with reasonable pore structures and porosities. For $D_{\text{particle}} > 50$ nm, curvature effects on overall particle is negligible.³⁴ The dominant mechanism on MSNP charging is found to be the EDL overlap inside the pores, which can be simply characterized by λ/D_{pore} . High EDL overlap yields high electric potential inside the pores close to the zeta potential of remaining solid parts; hence, the average MSNP zeta potential remain very close to predictions of flat plate theory. On the other hand, with the decrease in EDL overlap, pore electric potential decreases and becomes lower than solid zeta potential that the MSNP zeta potential diverges from existing theory. Second, three-dimensional porosity determines number of pores on the MSNP surface and their influence on surface charging. Porosity is also related with pore size that increase of porosity may due to increase of D_{pore} which also eventually decreases the EDL overlap. As a result, MSNP zeta potential becomes different than the flat plate theory predictions by increasing porosity and decreasing EDL overlap that we normalized results as a function of the nondimensional group of $\epsilon_{3D}(D_{\text{pore}}/\lambda)$ in Figure 11.

We present the results of $D_{\text{particle}} = 50$ nm with different D_{pore} , 3D porosity, and salt concentration from Figure 9a and b normalized by the flat plate theory in Figure 11. In addition, we added results of $D_{\text{particle}} = 330$ nm MSNP with different conditions. A universal behavior is obtained in zeta potential variation of MSNP as a function of $\epsilon_{3D}(D_{\text{pore}}/\lambda)$. Overall, MSNP zeta potential remained similar to flat plate predictions for $\epsilon_{3D}(D_{\text{pore}}/\lambda) < 0.01$, while it decreases by increasing $\epsilon_{3D}(D_{\text{pore}}/\lambda)$ value.

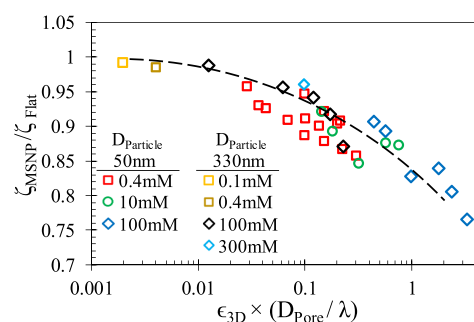


Figure 11. Average MSNP zeta potential normalized with flat surface theory as a function of 3D porosity, pore size, and EDL thickness for particle diameters of $D_p = 50$ and 330 nm.

4. CONCLUSION

We characterized the surface zeta potential of mesoporous silica nanoparticles of various pore sizes and porosities. In contrast to many studies considering the surface zeta potential as a material property that is independent of the particle properties, this study calculated the effects of porous properties. Using the numerical solution of ionic equilibrium based on PNP equation with CR boundaries, we found that the zeta potential around a MSNP strongly depends on pore size and porosity, in addition to the solution conditions. In this regard, we calculated the local electric potentials through the two-dimensional center line cross section of various MSNPs, and using these, we evaluated an average potential at the pore mouths and on the remaining particle surfaces. Through a systematic study, we evaluated a three-dimensional zeta potential for MSNPs with various conditions based on the ratio of the area covered by pore openings to the rest of the MSNP surface area. Results showed that electric potential at the surface pore openings are very different than the potential on the rest of the solid surfaces if the pore size is large and/or ionic salt concentration is high which corresponds to no EDL overlap case. Hence, the homogeneous surface zeta potential assumption is invalid even at this continuum level. As a function of three-dimensional porosity, the ratio of pore openings to MSNP surface area determines the influence of pore potentials; the average MSNP zeta potential can be up to 25% lower compared to the theoretical predictions for a flat plate. We characterized the variation of MSNP zeta potential in terms of pore size, porosity, and ionic condition by defining a nondimensional group as $\epsilon_{3D}(D_{\text{pore}}/\lambda)$. We observed a unified behavior through the results of different diameter particles at different porous and salt conditions as a function of $\epsilon_{3D}(D_{\text{pore}}/\lambda)$. For $\epsilon_{3D}(D_{\text{pore}}/\lambda) < 0.01$, MSNP zeta potential remains similar to flat plate predictions but decreases by increasing the $\epsilon_{3D}(D_{\text{pore}}/\lambda)$ value.

AUTHOR INFORMATION

Corresponding Author

Murat Barisik – Department of Mechanical Engineering, Izmir Institute of Technology, Izmir 35430, Turkey; orcid.org/0000-0002-2413-1991; Email: muratbarisik@iyte.edu.tr

Authors

Fetiye Esin Yakin – Biotechnology and Bioengineering Graduate Program, Izmir Institute of Technology, Izmir 35430, Turkey
Tumcan Sen – Department of Mechanical Engineering, Izmir Institute of Technology, Izmir 35430, Turkey

Complete contact information is available at:
<https://pubs.acs.org/10.1021/acs.jpcc.0c04602>

Notes

The authors declare no competing financial interest.

ACKNOWLEDGMENTS

This work was supported by the Scientific and Technological Research Council of Turkey (TÜBİTAK) under the Grant Number 118M710. Authors would like to thank Center for Scientific Computation at Southern Methodist University. This work was also supported by the BAGEP Award of the Science Academy.

REFERENCES

- (1) Slowing, I. I.; et al. Mesoporous Silica Nanoparticles for Drug Delivery and Biosensing Applications. *Adv. Funct. Mater.* **2007**, *17* (8), 1225–1236.
- (2) Chen, Z.; et al. Stimulus-response mesoporous silica nanoparticle-based chemiluminescence biosensor for cocaine determination. *Biosens. Bioelectron.* **2016**, *75*, 8–14.
- (3) Kang, M. S.; et al. Optical imaging and anticancer chemotherapy through carbon dot created hollow mesoporous silica nanoparticles. *Acta Biomater.* **2017**, *55*, 466–480.
- (4) Lee, C.-H.; et al. Near-Infrared Mesoporous Silica Nanoparticles for Optical Imaging: Characterization and In Vivo Biodistribution. *Adv. Funct. Mater.* **2009**, *19* (2), 215–222.
- (5) Tarn, D.; et al. Mesoporous silica nanoparticle nanocarriers: biofunctionality and biocompatibility. *Acc. Chem. Res.* **2013**, *46* (3), 792–801.
- (6) Cha, B. G.; Kim, J. Functional mesoporous silica nanoparticles for bio-imaging applications. *Wiley Interdiscip. Rev. Nanomed. Nanobiotechnol.* **2019**, *11* (1), No. e1515.
- (7) Chen, Y.; Chen, H.; Shi, J. In vivo bio-safety evaluations and diagnostic/therapeutic applications of chemically designed mesoporous silica nanoparticles. *Adv. Mater.* **2013**, *25* (23), 3144–76.
- (8) Jafari, S.; et al. Mesoporous silica nanoparticles for therapeutic/diagnostic applications. *Biomed. Pharmacother.* **2019**, *109*, 1100–1111.
- (9) Slowing, I. I.; Vivero-Escoto, J. L.; Trewyn, B. G.; Lin, V. S.-Y. Mesoporous silica nanoparticles: structural design and applications. *J. Mater. Chem.* **2010**, *20* (37), 7924.
- (10) Zhang, T.; et al. Synthesis of Podlike Magnetic Mesoporous Silica Nanochains for Use as Enzyme Support and Nanostirrer in Biocatalysis. *ACS Appl. Mater. Interfaces* **2020**, *12* (15), 17901–17908.
- (11) Watermann, A.; Brieger, J. Mesoporous Silica Nanoparticles as Drug Delivery Vehicles in Cancer. *Nanomaterials* **2017**, *7* (7), 189.
- (12) Chen, W.; et al. Nanomachines and Other Caps on Mesoporous Silica Nanoparticles for Drug Delivery. *Acc. Chem. Res.* **2019**, *52* (6), 1531–1542.
- (13) Chen, J.-F.; et al. Preparation and characterization of porous hollow silica nanoparticles for drug delivery application. *Biomaterials* **2004**, *25* (4), 723–727.
- (14) Castillo, R. R.; et al. Advances in mesoporous silica nanoparticles for targeted stimuli-responsive drug delivery: an update. *Expert Opin. Drug Delivery* **2019**, *16* (4), 415–439.
- (15) Luo, L.; et al. Monodisperse mesoporous silica nanoparticles of distinct topology. *J. Colloid Interface Sci.* **2017**, *495*, 84–93.
- (16) dos Santos, S. M. L.; et al. Synthesis and characterization of ordered mesoporous silica (SBA-15 and SBA-16) for adsorption of biomolecules. *Microporous Mesoporous Mater.* **2013**, *180*, 284–292.
- (17) Zhou, Y.; et al. Mesoporous silica nanoparticles for drug and gene delivery. *Acta Pharm. Sin. B* **2018**, *8* (2), 165–177.
- (18) Manzano, M.; Vallet-Regí, M. Mesoporous Silica Nanoparticles for Drug Delivery. *Adv. Funct. Mater.* **2020**, *30* (2), 1902634.
- (19) Argyo, C.; et al. Multifunctional Mesoporous Silica Nanoparticles as a Universal Platform for Drug Delivery. *Chem. Mater.* **2014**, *26* (1), 435–451.
- (20) Lu, J.; et al. Biocompatibility, biodistribution, and drug-delivery efficiency of mesoporous silica nanoparticles for cancer therapy in animals. *Small* **2010**, *6* (16), 1794–805.
- (21) Zhang, Q.; et al. Multifunctional Mesoporous Silica Nanoparticles for Cancer-Targeted and Controlled Drug Delivery. *Adv. Funct. Mater.* **2012**, *22* (24), 5144–5156.
- (22) Chen, F.; et al. In vivo tumor targeting and image-guided drug delivery with antibody-conjugated, radiolabeled mesoporous silica nanoparticles. *ACS Nano* **2013**, *7* (10), 9027–39.
- (23) Kim, M. J.; Ryoo, R. Synthesis and Pore Size Control of Cubic Mesoporous Silica SBA-1. *Chem. Mater.* **1999**, *11* (2), 487–491.
- (24) Trewyn, B. G.; Whitman, C. M.; Lin, V. S. Y. Morphological Control of Room-Temperature Ionic Liquid Templated Mesoporous Silica Nanoparticles for Controlled Release of Antibacterial Agents. *Nano Lett.* **2004**, *4* (11), 2139–2143.
- (25) Zhang, K.; et al. Facile large-scale synthesis of monodisperse mesoporous silica nanospheres with tunable pore structure. *J. Am. Chem. Soc.* **2013**, *135* (7), 2427–30.
- (26) Cauda, V.; Argyo, C.; Schlossbauer, A.; Bein, T. Controlling the delivery kinetics from colloidal mesoporous silica nanoparticles with pH-sensitive gates. *J. Mater. Chem.* **2010**, *20* (21), 4305.
- (27) Yu, T.; et al. Influence of geometry, porosity, and surface characteristics of silica nanoparticles on acute toxicity: their vasculature effect and tolerance threshold. *ACS Nano* **2012**, *6* (3), 2289–301.
- (28) Su, J.; Guo, H. Translocation of a charged nanoparticle through a fluidic nanochannel: the interplay of nanoparticle and ions. *J. Phys. Chem. B* **2013**, *117* (39), 11772–9.
- (29) Su, J.; Olvera de la Cruz, M.; Guo, H. Solubility and transport of cationic and anionic patterned nanoparticles. *Phys. Rev. E Stat. Nonlin. Soft Matter Phys.* **2012**, *85* (1), 011504.
- (30) Yeh, L.-H.; et al. Field Effect Control of Surface Charge Property and Electroosmotic Flow in Nanofluidics. *J. Phys. Chem. C* **2012**, *116* (6), 4209–4216.
- (31) Das, P. K. Effect of thermodiffusion on pH-regulated surface charge properties of nanoparticle. *Electrophoresis* **2016**, *37* (2), 347–55.
- (32) Fogolari, F.; Brigo, A.; Molinari, H. The Poisson-Boltzmann equation for biomolecular electrostatics: a tool for structural biology. *J. Mol. Recognit.* **2002**, *15* (6), 377–92.
- (33) Grochowski, P.; Trylska, J. Continuum molecular electrostatics, salt effects, and counterion binding—a review of the Poisson-Boltzmann theory and its modifications. *Biopolymers* **2008**, *89* (2), 93–113.
- (34) Barisik, M.; et al. Size Dependent Surface Charge Properties of Silica Nanoparticles. *J. Phys. Chem. C* **2014**, *118* (4), 1836–1842.
- (35) Alan, B. O.; Barisik, M.; Ozcelik, H. G. Roughness Effects on the Surface Charge Properties of Silica Nanoparticles. *J. Phys. Chem. C* **2020**, *124* (13), 7274–7286.
- (36) Abbas, Z.; et al. Size-Dependent Surface Charging of Nanoparticles. *J. Phys. Chem. C* **2008**, *112* (15), 5715–5723.
- (37) Shi, Y.-R.; et al. Experimental Determination of Particle Size-Dependent Surface Charge Density for Silica Nanospheres. *J. Phys. Chem. C* **2018**, *122* (41), 23764–23771.
- (38) Kobayashi, M.; et al. Aggregation and charging of colloidal silica particles: effect of particle size. *Langmuir* **2005**, *21* (13), 5761–9.
- (39) Namjesnik, D.; et al. Application of the surface potential data to elucidate interfacial equilibrium at ceria/aqueous electrolyte interface. *Adsorption* **2016**, *22* (4–6), 825–837.
- (40) Abendroth, R. Surface charge development of porous silica in aqueous solution. *J. Phys. Chem.* **1972**, *76* (18), 2547–2549.
- (41) Salis, A.; et al. Ion specific surface charge density of SBA-15 mesoporous silica. *Langmuir* **2010**, *26* (4), 2484–90.
- (42) Jiang, Z.; Stein, D. Charge regulation in nanopore ionic field-effect transistors. *Phys. Rev. E Stat Nonlin Soft Matter Phys.* **2011**, *83* (3), 031203.

- (43) Atalay, S.; et al. Surface Charge of a Nanoparticle Interacting with a Flat Substrate. *J. Phys. Chem. C* **2014**, *118* (20), 10927–10935.
- (44) Ninham, B. W.; Parsegian, V. A. Electrostatic potential between surfaces bearing ionizable groups in ionic equilibrium with physiologic saline solution. *J. Theor. Biol.* **1971**, *31* (3), 405–428.
- (45) Chapel, J. P. Electrolyte Species Dependent Hydration Forces between Silica Surfaces. *Langmuir* **1994**, *10* (11), 4237–4243.
- (46) Shubin, V. E.; Kékicheff, P. Electrical Double Layer Structure Revisited via a Surface Force Apparatus: Mica Interfaces in Lithium Nitrate Solutions. *J. Colloid Interface Sci.* **1993**, *155* (1), 108–123.
- (47) Butt, H.-J. Measuring electrostatic, van der Waals, and hydration forces in electrolyte solutions with an atomic force microscope. *Biophys. J.* **1991**, *60* (6), 1438–1444.
- (48) Popa, I.; et al. Importance of charge regulation in attractive double-layer forces between dissimilar surfaces. *Phys. Rev. Lett.* **2010**, *104* (22), 228301.
- (49) Huang, K.-D.; Yang, R.-J. Electrokinetic behaviour of overlapped electric double layers in nanofluidic channels. *Nanotechnology* **2007**, *18*, 115701.
- (50) Hughes, C.; Yeh, L.-H.; Qian, S. Field Effect Modulation of Surface Charge Property and Electroosmotic Flow in a Nanochannel: Stern Layer Effect. *J. Phys. Chem. C* **2013**, *117* (18), 9322–9331.
- (51) Sen, T.; Barisik, M. Slip Effects on Ionic Current of Viscoelectric Electroviscous Flows through Different Length Nanofluidic Channels. *Langmuir* **2020**, *36*, 9191.
- (52) Yeh, L. H.; Zhang, M.; Qian, S. Ion transport in a pH-regulated nanopore. *Anal. Chem.* **2013**, *85* (15), 7527–34.
- (53) Yeh, L. H.; et al. Tuning ion transport and selectivity by a salt gradient in a charged nanopore. *Anal. Chem.* **2014**, *86* (5), 2681–6.
- (54) Ai, Y.; et al. Effects of Electroosmotic Flow on Ionic Current Rectification in Conical Nanopores. *J. Phys. Chem. C* **2010**, *114* (9), 3883–3890.
- (55) Zeng, Z.; et al. Ion transport and selectivity in biomimetic nanopores with pH-tunable zwitterionic polyelectrolyte brushes. *Nanoscale* **2015**, *7* (40), 17020–9.
- (56) Yeh, L.-H.; Chen, F.; Chiou, Y.-T.; Su, Y.-S. Anomalous pH-Dependent Nanofluidic Salinity Gradient Power. *Small* **2017**, *13* (48), 1770253.
- (57) Peng, P. H.; et al. Thermal Dependence of the Mesoscale Ionic Diode: Modeling and Experimental Verification. *ACS Appl. Mater. Interfaces* **2020**, *12* (14), 17139–17146.
- (58) Sen, T.; Barisik, M. Internal surface electric charge characterization of mesoporous silica. *Sci. Rep.* **2019**, *9* (1), 137.
- (59) Sen, T.; Barisik, M. Pore connectivity effects on the internal surface electric charge of mesoporous silica. *Colloid Polym. Sci.* **2019**, *297* (10), 1365–1373.
- (60) Hill, R. J. Corona charge regulation in nanoparticle electrophoresis. *Proc. R. Soc. London, Ser. A* **2015**, *471*, 20150522.
- (61) Ozcelik, H. G.; Barisik, M. Electric charge of nanopatterned silica surfaces. *Phys. Chem. Chem. Phys.* **2019**, *21* (14), 7576–7587.
- (62) Beck, J. S.; et al. A new family of mesoporous molecular sieves prepared with liquid crystal templates. *J. Am. Chem. Soc.* **1992**, *114* (27), 10834–10843.
- (63) Kresge, C. T.; et al. Ordered mesoporous molecular sieves synthesized by a liquid-crystal template mechanism. *Nature* **1992**, *359* (6397), 710–712.
- (64) Kleitz, F.; Hei Choi, S.; Ryoo, R. Cubic Ia3d large mesoporous silica: synthesis and replication to platinum nanowires, carbon nanorods and carbon nanotubes. *Chem. Commun. (Cambridge, U. K.)* **2003**, No. 17, 2136–7.
- (65) Zhao, D.; et al. Triblock Copolymer Syntheses of Mesoporous Silica with Periodic 50 to 300 Angstrom Pores. *Science* **1998**, *279* (5350), 548–552.
- (66) Zhao, D.; et al. Nonionic Triblock and Star Diblock Copolymer and Oligomeric Surfactant Syntheses of Highly Ordered, Hydrothermally Stable, Mesoporous Silica Structures. *J. Am. Chem. Soc.* **1998**, *120* (24), 6024–6036.
- (67) Yu, C.; Yu, Y.; Zhao, D. Highly ordered large caged cubic mesoporous silica structures templated by triblock PEO–PBO–PEO copolymer. *Chem. Commun.* **2000**, No. 7, 575–576.
- (68) Kim, T.-W.; et al. Tailoring the Pore Structure of SBA-16 Silica Molecular Sieve through the Use of Copolymer Blends and Control of Synthesis Temperature and Time. *J. Phys. Chem. B* **2004**, *108* (31), 11480–11489.
- (69) Sakamoto, Y.; et al. Direct imaging of the pores and cages of three-dimensional mesoporous materials. *Nature* **2000**, *408* (6811), 449–53.
- (70) Narayan, R.; Nayak, U.; Raichur, A.; Garg, S. Mesoporous Silica Nanoparticles: A Comprehensive Review on Synthesis and Recent Advances. *Pharmaceutics* **2018**, *10* (3), 118.
- (71) Savic, S.; Vojisavljevic, K.; Pocuca-Nesic, M.; Zivojevic, K.; Mladenovic, M.; Knezevic, N. Hard Template Synthesis of Nanomaterials Based on Mesoporous Silica. *Metall. Mater. Eng.* **2018**, DOI: 10.30544/400.
- (72) Gobin, O. C. SBA-16 Materials Synthesis, Diffusion and Sorption Properties. Laval University, 2006; p 73.
- (73) Yeh, L.-H.; et al. Counterion condensation in pH-regulated polyelectrolytes. *Electrochem. Commun.* **2012**, *19*, 97–100.
- (74) Yeh, L. H.; et al. Controlling pH-regulated bionanoparticles translocation through nanopores with polyelectrolyte brushes. *Anal. Chem.* **2012**, *84* (21), 9615–22.
- (75) Yang, K. N.; et al. pH-responsive mesoporous silica nanoparticles employed in controlled drug delivery systems for cancer treatment. *Cancer Biol. Med.* **2014**, *11* (1), 34–43.
- (76) He, Q.; et al. A pH-responsive mesoporous silica nanoparticles-based multi-drug delivery system for overcoming multi-drug resistance. *Biomaterials* **2011**, *32* (30), 7711–20.
- (77) Popat, A. A pH-responsive drug delivery system based on chitosan coated mesoporous silica nanoparticles. *J. Mater. Chem.* **2012**, DOI: 10.7497/j.issn.2095-3941.2014.01.003.
- (78) Liu, J.; et al. Hollow mesoporous silica nanoparticles facilitated drug delivery via cascade pH stimuli in tumor microenvironment for tumor therapy. *Biomaterials* **2016**, *83*, 51–65.
- (79) Chen, Y.; et al. Multifunctional envelope-type mesoporous silica nanoparticles for pH-responsive drug delivery and magnetic resonance imaging. *Biomaterials* **2015**, *60*, 111–20.
- (80) Hill, S. J. Handbook of HPLC E. Katz, R. Eksteen, P. Schoenmakers and N. Miller (eds) Marcel Dekker, New York, 1998 xi?+?1000 pages. US \$225. ISBN 0-8247-9444-3. *Appl. Organomet. Chem.* **2000**, *14* (2), 130–131.
- (81) Zhuravlev, L. T. Surface characterization of amorphous silica—a review of work from the former USSR. *Colloids Surf., A* **1993**, *74* (1), 71–90.
- (82) Hair, M. L.; Hertl, W. Acidity of surface hydroxyl groups. *J. Phys. Chem.* **1970**, *74* (1), 91–94.
- (83) Leung, K.; Nielsen, I. M.; Criscenti, L. J. Elucidating the bimodal acid-base behavior of the water-silica interface from first principles. *J. Am. Chem. Soc.* **2009**, *131* (51), 18358–65.
- (84) Andersen, M. B.; et al. Streaming current and wall dissolution over 48 h in silica nanochannels. *J. Colloid Interface Sci.* **2011**, *360* (1), 262–71.
- (85) van der Heyden, F. H.; Stein, D.; Dekker, C. Streaming currents in a single nanofluidic channel. *Phys. Rev. Lett.* **2005**, *95* (11), 116104.
- (86) Andersen, M. B.; et al. Surface-dependent chemical equilibrium constants and capacitances for bare and 3-cyanopropyltrimethylchlorosilane coated silica nanochannels. *J. Colloid Interface Sci.* **2011**, *353* (1), 301–10.
- (87) Brown, M. A. Determination of Surface Potential and Electrical Double-Layer Structure at the Aqueous Electrolyte-Nanoparticle Interface. *Phys. Rev. X* **2016**, DOI: 10.1103/PhysRevX.6.011007.
- (88) Sen, T.; Barisik, M. Size dependent surface charge properties of silica nano-channels: double layer overlap and inlet/outlet effects. *Phys. Chem. Chem. Phys.* **2018**, *20* (24), 16719–16728.